PHYSICAL REVIEW D VOLUME 22, NUMBER 3 1 AUGUST 1980

Study of the Okubo-Zweig-Iizuka rule in exclusive photoproduction reactions

M. C. Goodman,* P. Avery, J. Butler,† G. Gladding, T. O'Halloran, J. J. Russell, A. Wattenberg, and J. Wiss
Department of Physics, University of Illinois, Urbana, Illinois 60801

M. Binkley, J. Cumalat, I. Gaines, M. Gormley, R. L. Loveless,‡ and J. Peoples
Fermi National Accelerator Laboratory, Batavia, Illinois 60510§

M. S. Atiya, S. D. Holmes, B. C. Knapp, W. Lee, and W. Wisniewski
Department of Physics, Columbia University, New York, New York 10027

(Received 12 March 1980)

A study of the Okubo-Zweig-Iizuka (OZI) rule has been performed in a high-energy photon beam by comparing the production ratios of exclusive meson final states. Measurement of the ratio $\sigma(\gamma A \to \phi\pi^+\pi^-A)/\sigma(\gamma A \to \omega\pi^+\pi^-A) = 0.10 \pm 0.02$ is evidence that the OZI rule does not suppress this photoproduction reaction to the extent observed in ϕ decays and in production by hadrons. The ratios of other exclusive photoproduction reactions are also presented.

I. INTRODUCTION

The Okubo-Zweig-Iizuka rule[1-3] (OZI rule or quark-line rule) was proposed to explain the suppressed decay of the ϕ meson into three pions. The picture is that the strange $s\bar{s}$ quarks of the ϕ are disconnected from the nonstrange quarks of the decay state and that disconnected diagrams are suppressed (or forbidden). The OZI rule was essential in explaining the narrowness of the newly discovered ψ states of the $c\bar{c}$ quarks[4,5] as well as the Υ family.[6,7] Its importance has generated a renewed interest in trying to understand the basis for the rule.

One of the questions that has arisen is whether or not the OZI rule applies to photon reactions. In particular there has been much interest in whether the OZI rule applies to production reactions the same way it does to decays. A number of exclusive hadroproduction experiments have found generally good agreement with OZI expectations for both the vector- and tensor-meson families.[8] One recent experiment, however, found a ratio for the reactions $(\pi^-p \to \phi\phi n)/(\pi^-p \to K^+K^-\phi n)$ which seemed too high.[9] In addition, inclusive production of ϕ and ψ mesons are generally not accompanied by K's or D's (Refs. 10, 11) although the implications for the OZI rule are less clear in this case.[12] Okubo has proposed e^+e^- experiments to study the question of the applicability of the OZI rule to photons.[13]

The photon is pictured as a superposition of $u\bar{u}$, $d\bar{d}$, $s\bar{s}$, $c\bar{c}$, etc., quarks weighted by the squares of the charges. For many processes, diffractive photoproduction gives results similar to those in e^+e^- reactions.

In the course of an extensive set of photoproduction experiments using the broad-band neutral beam at Fermilab, we acquired data which allowed us to investigate the applicability of the rule to photoproduction reactions. Specifically, this paper reports on the exclusive photoproduction of four-, five-, and six-body final states which can serve as a test of the OZI rule by comparing mesonic states containing various numbers of strange and nonstrange quarks.

The apparatus is described in Sec. II where the neutral beam, the momentum spectrometer, and methods for particle identification are discussed. The Cherenkov counters used for K and p identification and the lead-glass array used to detect π^0 mesons are especially important for ϕ and ω. Section III describes the data analysis. The results are presented in Sec. IV and are discussed in Sec. V.

II. DETECTOR

The experiment was conducted in the broad-band neutral beam at Fermilab in the east area of the proton laboratory. A schematic diagram of the detection apparatus is shown in Fig. 1. Table I contains a list of the apparatus elements and the abbreviations that are frequently used in the text.

A. The beam

The beam was produced from the 0° neutral secondaries resulting from a 400-GeV primary proton beam striking a beryllium target (350 mm long, 1.5 mm wide, 7.6 mm high). The charged particles were bent into a dump by sweeping magnets, leaving a beam made up of neutrons, photons, and some K_L^0's.

The neutral beam then passed through 34 m of liquid deuterium. The deuterium has a small ratio of interaction length to radiation length, which caused a reduction in the neutron-to-photon ratio by about a factor of 200, and a reduction in the

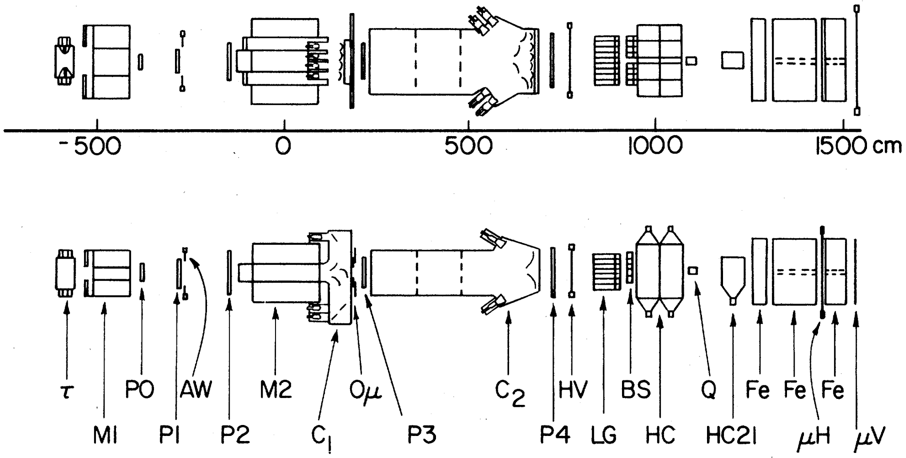

FIG. 1. A plan view (top) and elevation view (bottom) of the detector. Magnets $M1$ and $M2$ bend vertically.

K_L^0-to-photon ratio by about a factor of 2.

The size of the photon beam was determined by two fixed-aperture collimators. The apertures used for this experiment gave a 4 cm×4 cm beam spot on the photon target. Fixed- and variable-aperture collimators reduced the beam halo and are shown in Fig. 2. Sweeping magnets and steel shielding around the beam were placed at several locations in the 120-m-long neutral beam, in order to reduce the muon flux in the detector area.

The primary-proton-beam intensities varied from 3 to 9×10^{11} protons per pulse over a one sec-

TABLE I. Equipment.

Multiwire proportional chambers (PWC's)

Chamber	Size
$P0$	28.8 cm × 37.7 cm
$P1$	51.2 cm × 75.3 cm
$P2$	76.8 cm × 113.0 cm
$P3$	83.2 cm × 113.0 cm
$P4$	100.8 cm × 150.6 cm

$P1$, $P2$, $P3$, and $P4$ had time recorder modules (TRM's)

	Name	Number of tubes
Target counters	τ	20[a,b]
Cherenkov counter in magnet	C_1	12[a,b]
Large Cherenkov counter	C_2	16[a,b]
Wide veto counters	AW	4[a]
Beam veto counter	$A0$	1[a]
Upstream veto counters	$A\mu$	6[a]
Trigger counters	H,V	20[a]
Lead-glass counters	LG	90[b]
Back shower counters	BS	8[b]
Hadron calorimeter	HC	21[b]
Muon counters	$\mu H,\mu V$	40[a]

Magnets

Cornell magnet	$M1$ aperture:	35.6 cm × 76.2 cm
BM109 magnet	$M2$ aperture:	50.8 cm × 61.0 cm

[a] Counted in coincidence register (CR).

[b] Pulse height recorded in analog-to-digital converter (ADC).

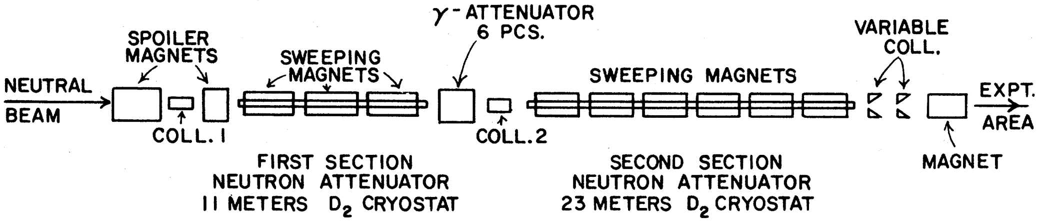

FIG. 2. Components of the neutral beam.

ond spill. The proton intensity was recorded using a secondary-emission monitor located 6 m upstream of the proton target. The proton-beam targeting location was monitored using segmented-wire ion chambers.

The integrated power of the photon beam was recorded on a pulse-by-pulse basis by a Wilson-type quantameter. It sampled ionization with 27 discs of lead 0.64 cm thick (a total of 1.25 interaction lengths and 31 radiation lengths). The quantameter was calibrated with a larger quantameter which had been extensively studied.[14] The resulting calibration constant was 7300 ions per GeV.

In order to measure the photon spectrum two methods were employed. The first method measured e^+e^- pairs in the spectrometer from a thin target. The second method used a lead-glass block placed in the beam with reduced intensity. The photon spectrum thus obtained is shown in Fig. 3. The two methods agreed that the photon spectrum was exponentially falling with a slope of 47 ± 3 GeV^{-1} in the energy range 0 to 200 GeV.

B. The target

The photon target consisted of 20 1-mm-thick pieces of scintillator 7.5 cm square, separated from each other by thin aluminum foil. The total thickness of the target was 22 mm which is 5% of a radiation length and 3% of an interaction length of material. (The noninteracting photon beam passed through another 4% of a radiation length and 2.5% of an interaction length of material before reaching the quantameter.) By weight, the target consisted of 91% carbon, 8% hydrogen, and 1% aluminum and was designed to detect the decays of intermediate-lifetime (10^{-12} s) particles. The pulse height in each target segment was proportional to the number of minimum ionizing particles in the counter. A systematic rise in pulse height downstream of the interaction point would be evidence for such a decay. The counter was also useful to check if the number of charged particles produced in the target matched the number of tracks seen in the spectrometer. The counters were calibrated using single muons and electron pairs and were checked in the data with ρ-meson events.

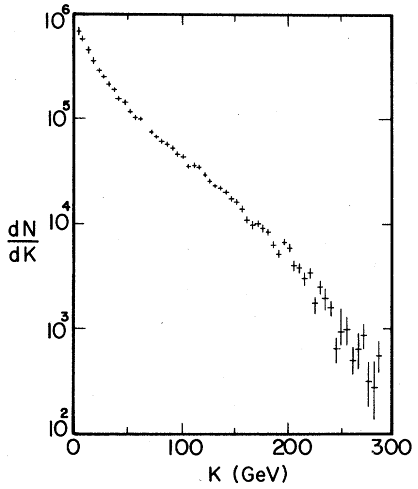

FIG. 3. The photon spectrum.

C. Momentum spectrometer

Momentum analysis was provided by two magnets and 15 planes of wires which were grouped in five chambers. The tracks in the spectrometer were separated into two categories: "inner-detector tracks" and "outer-detector tracks." A particle which passed through all five proportional chambers was called an "inner-detector track." These particles passed through both magnets ($M1$,$M2$) with vertical-momentum changes of 0.401 and 0.642 GeV/c, respectively. Particles going through $M1$ and $P0$–$P2$ but not $M2$ were called "outer-detector tracks." To determine momenta in the outer detector, tracks were projected through $M1$ to a vertex formed by two or more inner detector tracks. The angular horizontal acceptance of the inner detector and the outer detector were ±30 and ±60 mrad, respectively.

Each proportional wire chamber (PWC) had three signal planes labeled X, V, and U. The X wires were vertical, and the U and V wires were 11° from the horizontal. The wire spacing in a plane was 2 mm except in $P0$ where it was 1 mm and the X plane of $P4$ where it was 3 mm. The momentum resolution $\Delta p/p$ is proportional to momentum. For the inner detector $\Delta p/p$ was about $\pm 2.5\%$ at 100 GeV and for the outer detector $\pm 7.9\%$ at 100 GeV. For track energies lower than 5 GeV, errors in tracing tracks through the magnetic fields limited the momentum resolution. In order to understand the magnetic fields in $M1$ and $M2$, the fields were mapped with a sophisticated search coil system on an aluminum track that took measurements at 20 000 points in each magnet.[15]

In the PWC's (except $P0$), bands of 8 to 32 wires were grouped together and connected to time-recording modules (TRM's). There were 32 TRM's in each chamber, and for each hit a drift time relative to the signal from the target counter was recorded. The TRM information was used to improve the position resolution.

The TRM's were also counted to give an estimate of the charged-track multiplicity for triggering. The sum was calculated for each of the 15 planes, then a median for each chamber was determined. The lower of the multiplicities in $P3$ and $P4$ was called the inner-detector multiplicity while the median of $P0$, $P1$, and $P2$ was the inner-plus-outer multiplicity. Although $P0$ did not have TRM's, multiplicity signals were produced from the individual sense wires.

A separate, more complicated "X logic" was also performed on the TRM signals from the five X planes. Here the signals were divided into left and right regions, with a 5-cm gap in the middle excluded to eliminate electron pairs. This X logic was used in some triggers to demand at least two tracks in the spectrometer outside the electron pair region.

D. Cherenkov counters

The particle-identification system consisted of two Cherenkov counters (C_1 and C_2) which separated charged π-mesons, K mesons, electrons, and protons in various regions of momentum.

The first Cherenkov counter, C_1, which was in the magnet $M2$, had 12 RCA 4522 tubes and was filled with nitrogen at atmospheric pressure. The largest Cherenkov cone at the first mirror plane was 5.8 cm, but because the particles were bending in the magnet, and because the horizontal and vertical focusing were done in separate mirror planes, the light sharing at the phototubes was quite complicated. A $\beta = 1$ particle produced eight photoelectrons from the photocathode of a tube if all of the light cone was aimed at that one tube. The pion threshold was 6 GeV.

Figure 4 shows the top view of C_1. The magnet gap was 50 cm. The central mirror was 10 cm wide, with side mirrors covering the remaining part of the aperture. Vertical separation took place at the second plane at mirrors which were 25 cm high. The distance from the first mirror to the second one was 100 cm. The length of the gas radiator in C_1 was 250 cm. Owing to the averaged differences in the horizontal and vertical focusing, the projection of the light cone had an elliptical shape at the face of the phototube.

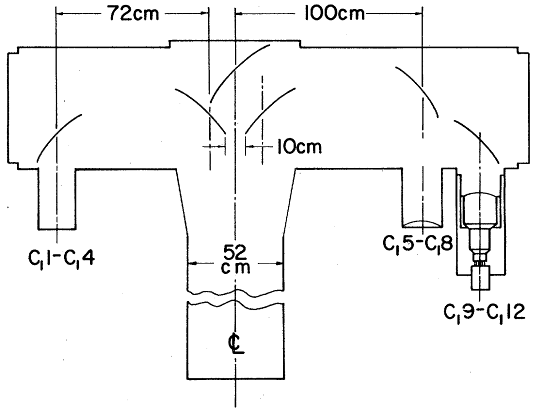

FIG. 4. Top view of the mirrors in C_1.

C_2 contained 16 spherical mirrors each viewed by a photomultiplier. A diagram of the vertical mirror positions in C_2 is shown in Fig. 5. C_2 was filled with a 20% nitrogen, 80% helium mixture and the index of refraction $n-1$ was 4.7×10^{-5}. The largest Cherenkov cone spread out 5.3 cm, and a particle well above threshold gave six photoelectrons. The pion threshold was 11 GeV. The momentum thresholds are listed in Table II and threshold curves are shown in Fig. 6.

The phototubes in the Cherenkov counters were monitored in several ways. Pulse heights were

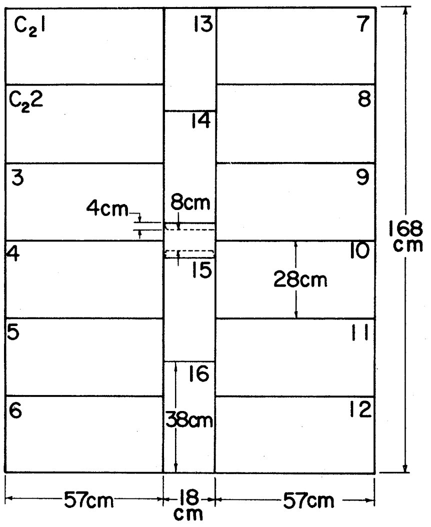

FIG. 5. Beam view of the mirrors in C_2.

TABLE II. Cherenkov thresholds (GeV).

	π	K	p
C_1	5.8	20.7	39.3
C_2	10.7	37.9	72.0

analyzed using electron runs and regular data runs and checked for constant gains. The tubes (RCA 8854) in C_2 had a bi-alkali photocathode and a gallium phosphide first dynode, so that the gain of the first stage was about 30. Therefore, one-photoelectron peaks could be monitored off-line very precisely by pulse-height-analyzing noise pulses.

E. Lead-glass array

The lead-glass block array, shown in Fig. 7, had a 10-cm gap through which electron pairs could pass. In the beam region, the blocks were 6.35 cm × 6.35 cm; outside the beam region the blocks were 15.2 cm × 15.2 cm. The small blocks were 46 cm long, or 18.1 radiation lengths and 1.4 interaction lengths. The large blocks were 58 cm long, or 20.4 radiation lengths and 1.8 interaction lengths. The energy resolution was $\Delta E/E = 2 + 5/E^{1/2}\%$. Figure 8 shows E/p (the ratio of the energy measured in the lead glass to the momentum measured in the spectrometer) for electrons at all energies from a calibration run. There were five periods of lead-glass calibrations during the experiment. A light-pulser system was used to monitor the stability of the phototubes. Light-pulser records were written on tape between spills and were used to correct lead-glass calibration constants on a run-by-run basis.

Behind the lead-glass array were eight lead-scintillator sandwich counters, which were used to detect neutral energy that went into the gap. These counters also detected showers that escaped from the edge of the lead-glass array into the slot. These counters had 10 cm of lead (16 radiation lengths) and were 51 cm wide, 15 cm high, and were placed 7 cm above and below the beam height.

F. Trigger electronics

Figure 9 shows an abbreviated schematic of the triggering and data-acquisition system. The type of events we were trying to collect had four or more charged particles inside our spectrometer. We wanted to avoid triggering on the copiously produced Bethe-Heitler e^+e^- pairs or the muons from upstream interactions in our beam line. Much of the triggering was "dc" in nature so that precise relative timing was not critical and there

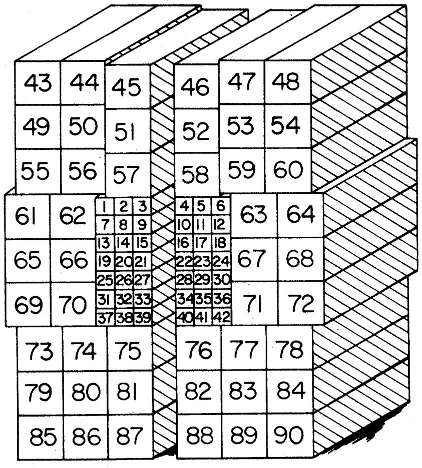

FIG. 7. The lead-glass array.

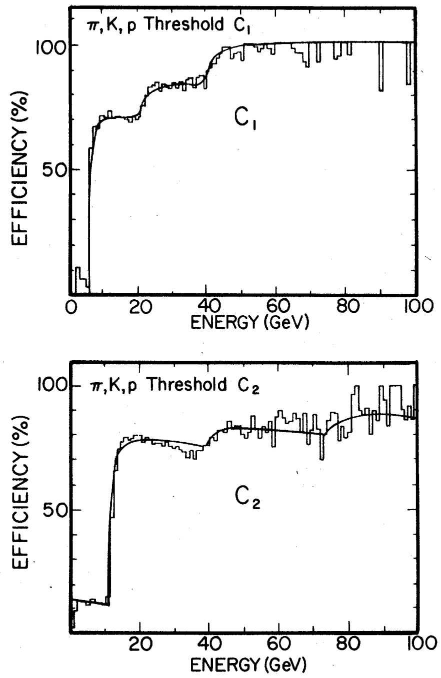

FIG. 6. Cherenkov threshold curves.

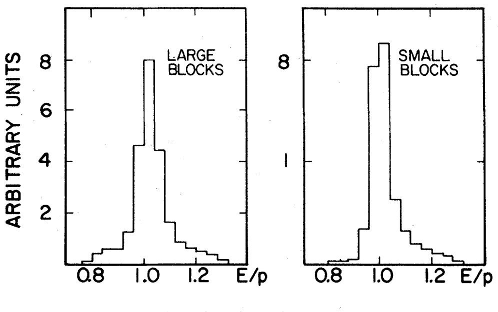

FIG. 8. Calibrated pulse height over spectrometer momentum using electrons in the lead glass.

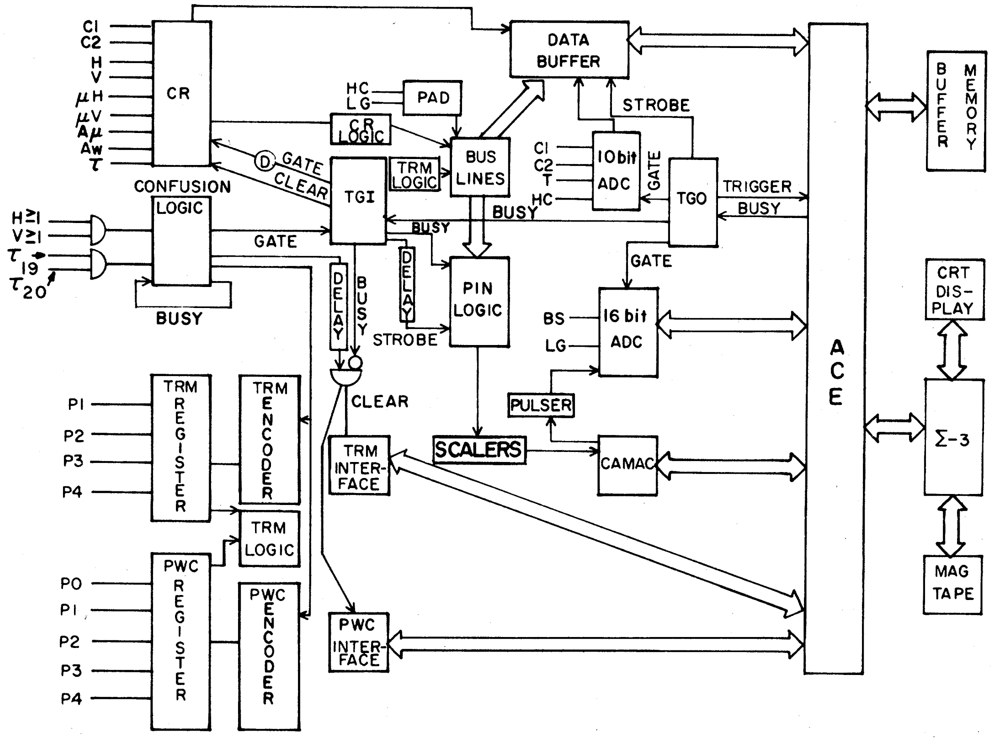

FIG. 9. Schematic of fast electronics and trigger.

was continuous scaling of trigger rates during event readout to monitor deadtime. High data-transfer rates were handled by an automatic system using its own data memory with no intervention from the on-line computer. The system could read in about 200 events of average length during a 1-s beam spill, limited by the size of the available buffer memory.

Signals from the trigger hodoscope (*H* and *V*) counters were discriminated to form an input into the master gate (MG). The other input to the master gate was a coincidence between the last two target counters ($\tau 19$ and $\tau 20$). The signals forming the master gate were within a 15-ns window. This MG signal was scaled and the total was read by the computer after each beam pulse. The MG was used to gate the rest of the logic. If the logic was busy processing a previous MG then the MG was ignored. The ratio of the number of master gates accepted to the number generated was a measure of the logic live time, and was usually about 70%. Half of the deadtime was due to the MG and the other half came from the buffer memory being full.

An MG initiated a series of events using a second level of trigger logic which was dc in nature. Hits in scintillation counters were recorded in individual coincidence registers (CR's). Also TRM lines were counted and various combinations were used to generate logic levels. Finally signals from the lead-glass array and hadron calorimeter were read using a five-bit pulse-area digitizer for use in an energy-level trigger. A total of 16 signals from individual CR bits or from logical combinations were formed. These were placed on a 16-channel parallel bus which was connected into "pin-logic" cards. Each pin-logic card saw the 16 logic levels on the bus lines and compared the bus lines to 16 requirements set by jumper wires inside the card. Each of the 16 lines could be compared to "on," "off," and "don't care." A pin logic was satisfied if the bus lines agreed bit by bit with its internal requirements. Any card that was satisfied generated a trigger. If this occurred while the readout system was not busy, the event that caused it was read out into the buffer memory for copying onto magnetic tape.

G. Lepton identification

For calibration purposes, we could trigger on electron pairs which originated in a small lead converter upstream of our target, or we could take single muons originating from hadron decays near the primary target. These were useful to calibrate the multiplicity determination in the target scintillator counters. Electrons were identified as particles whose pulse height in the lead glass corresponded to their spectrometer momemtum.

The muon identifier included a steel shield 170 cm thick, a horizontal array of 22 scintillation counters (μ-H), another steel shield 65 cm thick, and a vertical array of 18 scintillation counters (μ-V). Each of the μ-V (μ-H) counters was 122 cm (91 cm) long, 20 cm wide, and 6.2 mm thick. Muons were identified by projecting tracks to each plane of counters and requiring that a counter within the multiple-scattering radii in each of the two hodoscopes be on.

H. Hadron background in the neutral beam

After the deuterium filter, neutral hadrons constituted the order of 1% or less of the number of photons with an energy above 50 GeV in the neutral beam. However, their interaction cross sections were much greater than the hadronic cross sections of the photon. These hadronic events constituted a considerable background for most inclusive and rare exclusive processes. Neutrons had an average energy near the primary proton energy and could often be excluded on an event-by-event basis with a high-energy cut. The average K_L energy was much more like that of the photon.

In order to independently measure the effect of this background, one-fourth of the data were taken with the photon beam attenuated by six radiation lengths of lead. The attenuator was located between the two sections of deuterium shown in Fig. 2. These background data runs were taken with the same trigger conditions and analyzed with the same programs that were used for the regular data. The relative normalization was fixed by the primary proton flux and corrected for the 17% hadron loss in the photon attenuator. Thus, at any stage of the analysis this background could be estimated and subtracted.

III. DATA ANALYSIS

A. Reconstruction

During the experiment, 1600 data tapes, each with about 20,000 events, were written. These events were first processed by a reconstruction program in which hits in the wire chambers were associated into tracks. In addition, there was a search for any pairs of tracks which intersected between the two upstream multiwire proportional chambers $P0$ and $P2$ but which did not project through $P0$. Track vectors before and after the bending magnet $M2$ were written out onto magnetic tape. Also at this stage, hits in the wire chambers were matched to hits in the time recorder modules (TRM's), and channels in the analog-to-digital converters (ADC's) whose pulse height were consistent with pedestal were deleted.

In the next stage of the analysis, the track vectors were refitted using positions in the chambers based on the TRM's. Hits in the Cherenkov counters C_1 and C_2 were used to determine whether each track which was above pion threshold emitted Cherenkov light in each counter. If possible a target vertex was located and possible K_S and Λ events were identified. Pulse heights in the lead-glass blocks were associated into showers.

B. Vertex identification

To find a target vertex, all inner-detector tracks were projected back through the magnet $M1$ to the center of the target. Using only tracks which projected to the target, a point of closest approach for this set of tracks was calculated. Tracks which projected less than 4.0 mm from this point were assigned to the main vertex. Leftover tracks were associated into secondary vertices which could be from V^0's, conversion electrons, or electron pairs. A plot of the distance of closest approach is shown in Fig. 10. The z distribution of the vertex thus obtained is plotted in Fig. 11.

Once a vertex was identified, a momentum for outer-detector tracks could be calculated by projecting the track from the bend point of $M1$ to the target vertex. If the projection in the nonbending plane was less than 4.3 mm from the vertex, the outer-detector track was assigned to the vertex. Using the reconstructed data, 86% of inner-detector tracks were assigned to a vertex in the target and 72% of the outer-detector tracks were assigned.

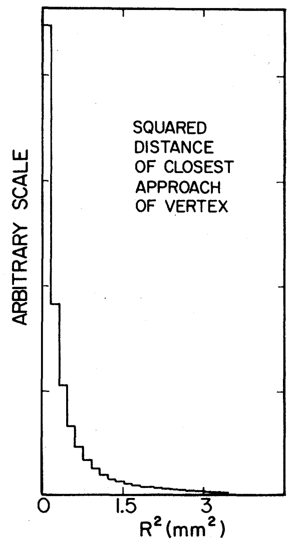

FIG. 10. Squared distance of closest approach described in the text.

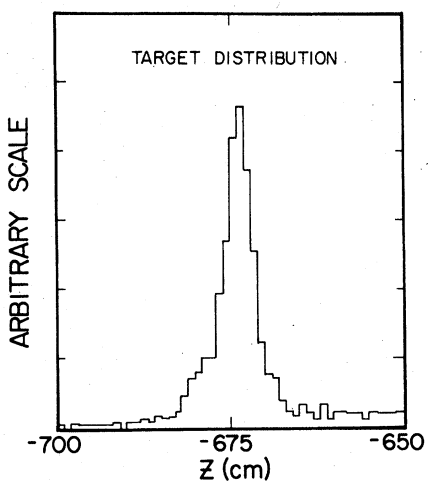

FIG. 11. Reconstructed target-vertex distribution.

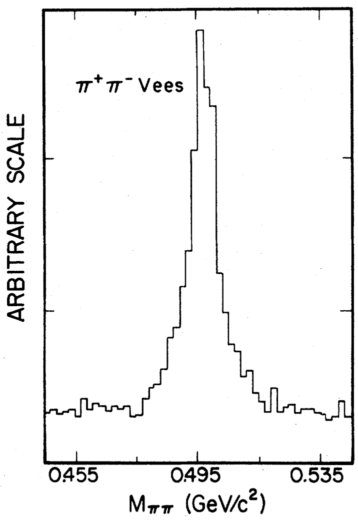

FIG. 12. The $\pi^+\pi^-$ mass spectrum for vees in the region of the K_S.

C. Vee identification

The V^0 candidates were separated into three classes depending upon the location of the intersection and whether the tracks were in the inner or outer detector.

The first class, the downstream V^0's which decay between $P0$ and $P2$, were identified during the reconstruction process. Each track had to trace through at least three consecutive chambers.

The tracks from V^0's which decayed before $P0$ were influenced by the magnet $M1$ so these V^0's were subdivided into groups which did and did not contain an outer-detector track. Most of the K_S's and half of the Λ's had two inner-detector tracks. They were required to have a distance of closest approach of less than 3.1 mm. For the case using one inner detector and one outer detector track, the intersection in the nonbend plane was required to be far from the target.

Using the assumption both particles are pions gives the K_S^0 mass plot shown in Fig. 12. When the higher-momentum track is called a proton, we see $\Lambda/\bar{\Lambda}$'s as shown in Fig. 13.

D. *K* identification

The Cherenkov system separated π's, K's, and p's in various momentum ranges but there was ambiguity whenever tracks shared Cherenkov mirrors or did not leave enough light in a counter for a firm on/off test. It was possible to identify unambiguously a particle in only a fraction of the cases. Therefore, it was desirable to resolve ambiguities in a way that identified correctly most of the K mesons in $K^+K^-\pi^+\pi^-$ events, but did not introduce large backgrounds from π's and protons.

The majority of the particles were π mesons. Therefore any track which was ambiguous as to π/K or $\pi/K/p$ was called a π. Any track with no Cherenkov information such as an outer-detector track was called a π. In the restricted momentum region that the Cherenkov counters could distinguish K's and p's, the measured K^+ (K^-) to proton (antiproton) ratio was 2.8 (3.9) so K/p tracks were called K's.

One way the efficiency of K-meson identification was measured was to use inclusive ϕ-meson production. The number of identified ϕ's using the Cherenkov counter was about $\frac{2}{3}$ the total number using a K hypothesis for all inner-detector tracks. This varied as a function of energy and multiplicity, but it suggests that the K identification efficiency was about 80%. In addition, the signal and

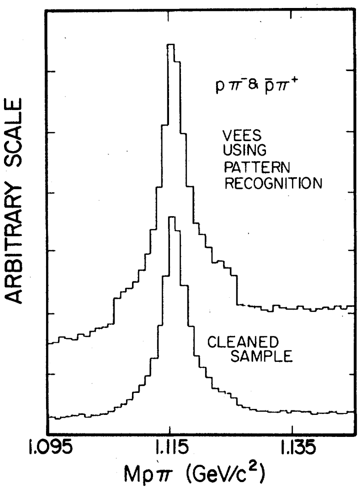

FIG. 13. The upper $p\pi$ mass spectrum uses all vees to get Λ^0's. The lower plot includes geometrical and Cherenkov cuts.

background events in the region of the ϕ were studied for each Cherenkov identification of the pair. For example, the signal to background was 0.66 for two tracks which could both be either a K or p, and it was less than 0.08 for two tracks when one was called a K and the other was called a π.

The number of π's that were called K's was less than a few percent. The π/K separation came from a track being on or off above the pion threshold. The pulse height required for an on identification in a phototube was about one-third of that from a single photoelectron. If the pulse height in a counter was below this value, the track was called "off" for those tracks where the expected average number of photoelectrons was at least 2.5. (A track which did not unambiguously satisfy either of these conditions was called "don't know.") For the vast majority of tracks we expected an average of more than five photoelectrons. The probability of 0 photoelectrons when the average is 5 is less than 1% for a Poisson distribution. However, protons may have accounted for 20–30% of the single tracks called K's.

The effect of these backgrounds in $K^+K^-\pi^+\pi^-$ events is further reduced. A state with odd strangeness or baryon number such as $K^+\pi^-\pi^+\pi^-$ would not have been photoproduced. These hadron-induced background events were subtracted using the background data discussed in Sec. II H. In a $\pi^+\pi^-\pi^+\pi^-$ event, the chance that two π's failed to count was very small. Also since the production of states which include a resonance such as $\phi\pi\pi$ and $K^*K\pi$ was calculated above the mass background continuum under each resonance, the channels which could contribute background were reduced or eliminated.

Backgrounds due to π contamination in the $KK\pi\pi$ sample were a different problem. Tracks which were π/K or $\pi/K/p$ were called π's, so there could be backgrounds from channels such as $KKKK$. However, most K's and p's were below the Cherenkov thresholds, so an event with four heavy particles was not prone to the confusion in the Cherenkov counter which would increase the ambiguous particle identifications. Also the $KKKK$ sample itself was measured to be a small fraction of the $KK\pi\pi$ sample.

The K^+K^- plot using identified K's is shown in Fig. 14. This figure also includes a plot of the mass calculated by taking K^+'s and K^-'s from different events and normalizing to the data. This seems to be a satisfactory way to determine the combinatoric background for this case.

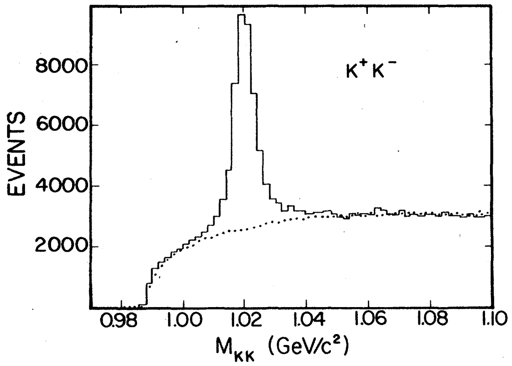

FIG. 14. Inclusive K^+K^- mass plot. The dashed line is described in the text.

E. π^0 detection

Neutral π's were detected using showers in the lead-glass array. A program associated struck blocks which were near to each other into candidate electromagnetic showers. The program then calculated the best position for the location of each shower and its energy. In addition, a position error was determined for each shower based on the amount of shower sharing between blocks and geometrical factors.

The position of each shower was compared to the projected position of spectrometer tracks and if the separation was less than 12 cm, the shower was associated with the track. The unassociated showers were then projected back to the target and momentum vectors for photon candidates were formed. The mass for each pair of photons was calculated and a π^0 candidate was tagged if $185 > M_{\gamma\gamma} > 85$ MeV/c^2. If a given shower was used in more than one candidate, the candidate with the higher energy was chosen. The $\gamma\gamma$ mass in four-charged-track events is shown in Fig. 15.

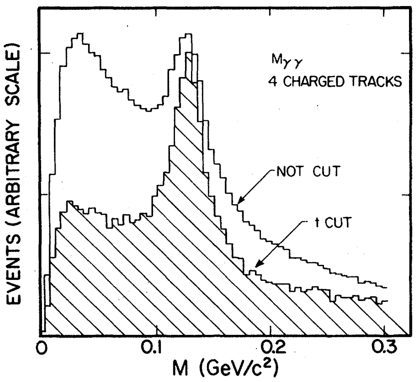

FIG. 15. Mass of $\gamma\gamma$ pairs in events with four charged tracks. The shaded area shows the improvement in the π^0 signal when the whole event is consistent with $|t| < 0.05$ GeV^2.

F. Monte Carlo programs

To calculate the acceptance and triggering efficiency for various states, a Monte Carlo program was developed.

In order to match the acceptance in the detector, only events above 60 GeV were generated. A typical reaction used in the Monte Carlo might have the following sequence:

$$\begin{tikzcd}[column sep=small] \gamma \arrow[r] & V \arrow[r] & ABC \arrow[dr] & \\ & & & DE\,, \end{tikzcd}$$

where the particles A, B, D, and E were long-lived particles and C was a resonance. The important kinematic variables that had to be chosen were the mass, energy, and p_T. The mass distribution M_V was thrown as a Gaussian 1 GeV wide. It peaked several hundred MeV above threshold and was cut off at threshold. The energy distribution was chosen to start at 60 GeV and to match the photon energy spectrum. This was equivalent to assuming that the cross section was independent of energy. The mass and energy distribution in the Monte Carlo matched the distributions in the data in every channel within statistics. The p_T distribution for V was chosen to reproduce only the coherent peak in the t distribution. A low-t cut was applied to the data and the acceptance does not vary as a function of t in this region so this procedure was adequate.

The parent V was then allowed to decay using a phase-space distribution $V \to ABC$. A Breit-Wigner distribution was used for the mass of the resonance $C \to DE$. The charged tracks were traced through the real field of the magnet $M1$, as determined by the magnetic measurements and then projected through the PWC's. The appropriate PWC hits and TRM times were generated and written out onto data records identical to the data records written during the experiment. The TRM's were used to set the trigger bus lines on or off.

The lead-glass ADC's were written out by projecting γ's to the lead glass and using shower sharing curves to divide up the pulse height among the various blocks. A pulse height for the hadron calorimeter was generated which was smeared by a Gaussian. Each pulse height in the target counter was smeared by a Landau distribution.

Hits in the Cherenkov counters were generated by using the fact that a low number (eight in C_1, six in C_2) of photoelectrons, N, was detected for a $\beta = 1$ track. Thus, after the appropriate N was calculated for each track, it was smeared by a Poisson distribution and then that number of photons was traced through the Cherenkov-counter geometry. The photons were projected from the particle trajectories in each counter and at the appropriate Cherenkov angle. The pulse height on each phototube was then smeared by a Gaussian.

Tapes generated by the Monte Carlos were processed with the same reconstruction, edit, and analysis programs as the data. In addition, events were required to satisfy the experimental trigger. In this way, geometrical acceptance, triggering efficiency, and the efficiency of all analysis programs (such as π^0 detection or K identification) were measured at the same time. For each final state, the percentage of generated events which passed all the cuts in the analysis program was called the "acceptance."

The acceptance could change from state to state for a number of reasons. For instance, when both K's were identified, the detection efficiency for the mass cut on ϕ's was 100% but for K^*'s, the mass cut was only 80% efficient.

IV. PRESENTATION AND DISCUSSION OF DATA

Using only charged tracks from the spectrometer and the Cherenkov counter for K identification 24 185 candidate $K^+K^-\pi^+\pi^-$ events were found. Then looking at the lead-glass array for π^0 identification, 5210 of these events became $K^+K^-\pi^+\pi^-\pi^0$ candidates. In a similar way, $K^+K^-\pi^+\pi^-\pi^+\pi^-$, $K^+K^-K^+K^-$, and $\pi^+\pi^-\pi^+\pi^-\pi^0$ events were selected. There were 7460, 1637, and 118 216 candidate events respectively. The ρ, K^*, ϕ, ω, and η content of these channels is discussed in Sec. IV A. The cuts used to identify coherent events are discussed in Sec. IV B. Background subtractions and corrections are presented in Sec. IV C. The ratios of production cross sections for various states are given in Sec. V.

A. ρ, K^*, ϕ, ω, and η content

Within the event samples $K^+K^-\pi^+\pi^-$, $K^+K^-\pi^+\pi^-\pi^0$, $\pi^+\pi^-\pi^+\pi^-\pi^0$, and $K^+K^-\pi^+\pi^-\pi^+\pi^-$ it was straightforward to determine the number of events from each of the subchannels $K^+K^-\rho$, $K^\pm\pi^\mp K^{*0}$, etc. The background under each resonance (ρ, K^*, etc.) was large, and it was not possible to determine a particular subchannel on an event-by-event basis. However, the backgrounds (nonresonant mass continua) were smooth, and it was possible to determine accurately the relative contribution for each by extrapolating the background curve under each resonance for the exclusive $K^+K^-\pi^+\pi^-$ sample. The $\pi^+\pi^-$, $K^\pm\pi^\mp$, and K^+K^- combination mass plots are shown in Figs. 16–18. Note that in the $\pi^+\pi^-$ and K^+K^- plots there is one combination per event while in the $K\pi$ plot there are two combinations per event. Clear peaks are seen for the ρ, K^* (890), and ϕ mesons. In Fig. 19 a mass plot is

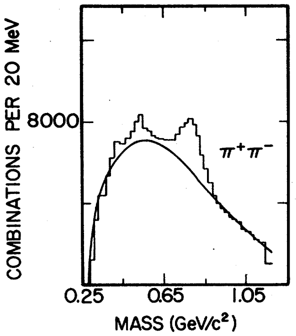

FIG. 16. $\pi^+\pi^-$ combinations from $K^+K^-\pi^+\pi^-$ events. The curve is an estimate of the background.

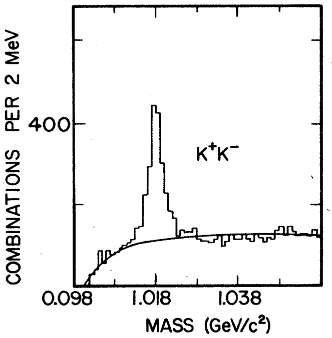

FIG. 18. K^+K^- combinations from $K^+K^-\pi^+\pi^-$ events. The curve is an estimate of the background.

presented for the $\pi^+\pi^-\pi^0$ combination from the $\pi^+\pi^-\pi^+\pi^-\pi^0$ sample. In this case there are four combinations for each event. The η and ω mesons are seen here.

For each subchannel, we define a "resonance efficiency parameter" ϵ_R, which is the fraction of events above the background within a suitable chosen mass cut. These parameters are determined separately for the regular data and the background runs. The parameters for each channel are listed in Table III. The dependence of ϵ_R was studied for its sensitivity to the background extrapolations. It was found that the largest variation was 5%.

B. Determination of coherent events

For studying the OZI rule for photon interactions, we were interested in events which had the properties of photons, which dissociated into hadrons, and in which the quantum state of the target nucleus was unchanged. Diffractive events which coherently scattered off the entire nucleus closely satisfied this requirement. Therefore we selected events with a small transverse momentum ($|t| \leq 0.05$ GeV^2), with no nuclear breakup or fragments, and with no detectable evidence of other particles.

These criteria also reduced the fraction of events that arose from the neutrons and K_L^0's in the beam. Although these neutral hadrons constituted the order of 1% or less of the number of photons above 50 GeV, their interaction cross sections were two orders of magnitude greater than the photon-hadron production cross sections. Without the coherent nuclear diffraction criteria, about half of the trigger events were initiated by the neutral hadrons in the beam.

The exclusive events of interest were required to have no hits in veto counters outside the spectrometer acceptance and to have not too many extra hits (<1.3 average per plane) in the wire chambers. The t cut was most important in reducing neutral-hadron events. The sample size was reduced by about a factor of 5 due to this cut. For the case of a four-particle event plus a nuclear recoil, t is determined as $t_{\min}+(\sum_i p_{xi})^2 +(\sum_i p_{yi})^2$. $t_{\min}$ is very small. For a final state with a mass of 4 GeV/c^2 and 60 GeV energy, $t_{\min}$ is $M^4/4E^2 = 0.02$ GeV^2. We cut at $|t| < 0.05$ GeV^2. As an example, the $|t|$ distribution for $KK\pi\pi$ events is shown in Fig. 20. The selection of K

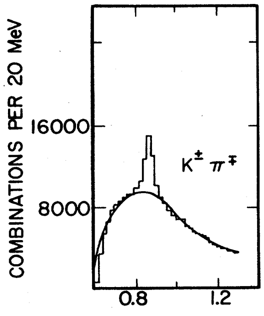

FIG. 17. $K^\pm\pi$ combinations from $K^+K^-\pi^+\pi^-$ events. The curve is an estimate of the background.

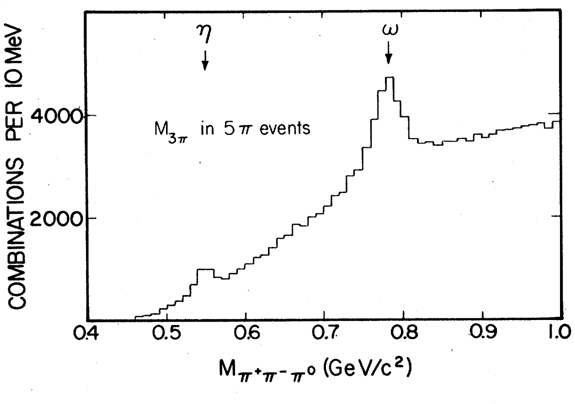

FIG. 19. Three-π mass combinations in five-π events.

TABLE III. Events by state—all cuts.

State	N_γ	ϵ_R	N_K	ϵ_R	C	N_{ev}	σ
$\phi\pi^+\pi^-$	234	0.53	39	0.52	2.54	72.9	13.3
$K^{*0}K^\pm\pi^\mp$	1136	0.26	124	0.27	2.54	212.4	19.3
$K^+K^-\rho$	964	0.24	126	0.19	2.54	167.3	15.0
$K^+K^-\pi^+\pi$	2187	1.00	288	1.00	2.54	1455	63.6
$K^{*\pm}K^\mp$	26	0.42	8	0.29	2.54	5.0	3.7
$K^{*0}K_s$	25	0.37	3	0.22	2.54	7.6	2.1
$K^\pm\pi^\mp K_s$	93	1.00	20	1.00	2.54	42.2	14.9
$\omega\pi^+\pi^-$	3477	0.25	512	0.14	2.57	685	47.5
$\eta\pi^+\pi^-$	321	0.32	38	0.11	2.57	92.0	7.9
ωK^+K^-	53	0.25	7	0.14	2.54	10.8	3.1
ηK^+K^-	9	0.32	1	0.11	2.54	2.6	1.0
$\phi\pi\pi\pi$	44	0.22	10	0.21	2.54	4.2	2.4
$KK\rho\pi$	140	0.10	21	0.08	2.54	9.4	1.8
$K^*K\pi\pi$	183	0.11	42	0.11	2.54	7.9	2.8
$KK\pi\pi\pi$	425	0.41	71	0.41	2.54	100.3	15.4
$\phi\pi\pi\pi\pi$	60	0.56	5	0.48	2.43	27.8	5.3
$K^*K\pi\pi\pi$	284	0.18	73	0.16	2.43	22.7	9.4
$KK\rho\pi\pi$	364	0.22	57	0.18	2.43	55.2	6.8
$KK\pi\pi\pi\pi$	446	1.00	89	1.00	2.43	229.7	31.2
$KKKK$	22	1.00	3	1.00	2.54	14.4	6.4
$KK\phi$	10	0.65	2	0.71	2.54	2.9	3.3
$\phi\phi$	2		0		2.54	2	2

events was discussed in Sec. III D.

To restrict ourselves to events with no nuclear breakup we used the segmented target counter (τ). Each segment past the interaction point usually gave a pulse height reflecting at least the number of minimum ionizing particles passing through it. An average (N_τ) was determined from the counters that were on. Because the interaction point could be anywhere in the first segment, that signal was disregarded; if at least three counters were still being used, the highest signal was also thrown out in order to minimize fluctuations. In inclusive particle production, the τ counters were not successful in predicting spectrometer multiplicities because of highly ionizing nuclear fragments, but in coherent photoproduction, they were useful because the momentum exchange was so small that the nucleus remained intact. Segment constants were normalized using electron and muon calibration data. An average N_τ plot for various hadronic final states after the t cut was applied is shown in Fig. 21. For four-charged-particle channels, the cut $N_\tau < 5$ was chosen.

Next, it was necessary to look in the lead-glass array for evidence of neutral particles. First, showers within 12 cm of a charged track were ignored. An attempt was then made to pair the

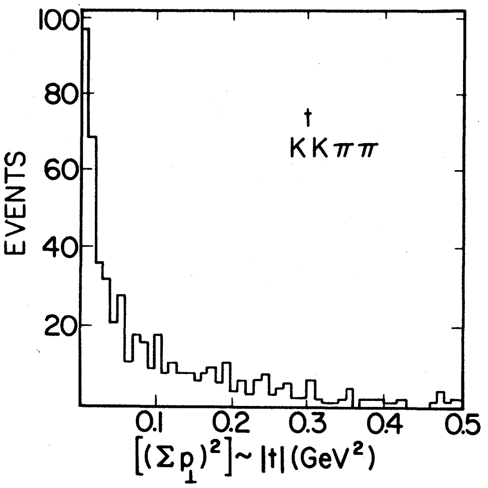

FIG. 20. t distribution for $KK\pi\pi$ events satisfying other cuts.

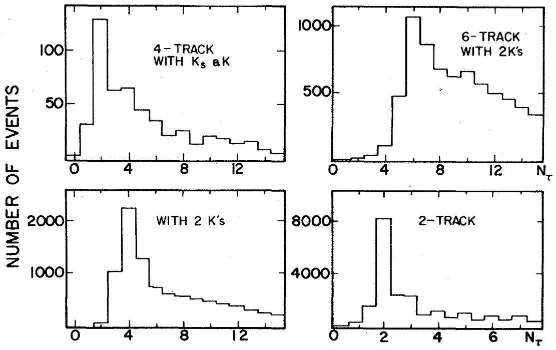

FIG. 21. Multiplicities measured by the 20-element target counter for various cases in the spectrometer.

other showers into π^0's. If a π^0 was found the event was removed from the "all charged particle" samples. The total of the remaining pulse height was the "unassociated neutral energy" (E_{un}) and if the total unassociated neutral energy was greater than 20 GeV, the event was thrown out.

There were some physics motivations for requiring no unassociated energy at all. This cut was left looser, however, because hadrons are known to leave energy within lead glass at a large distance from their tracks. A cut larger than 12 cm could have been employed, but this would have reduced the efficiency of π^0 identification. In addition, the probability of sampling information from another event was higher for the lead glass than for other detectors due to a larger gate width.

In order to study the quality of the π^0's, the analysis was carried out without a mass cut of the π^0 and that cut was applied last. Plots of the mass of $\gamma\gamma$ combinations before and after the diffractive cuts in the $K^+K^-\pi^+\pi^-\gamma\gamma$ sample are shown in Fig. 15. Notice that the diffractive cuts bring out a much better signal to background for the π^0 which is a very good indication that the events are really exclusive. Before these cuts, in the background events, there could be other γ rays from multiple π^0's.

Another indication of the presence of real diffractive events is that whichever cut is made first of t, N_τ, π^0 mass, or E_{un}, one finds a substantial number of events eliminated, while the cut made last eliminates only a few events. Table IV shows that the cuts are successful in increasing the ratio of $K^+K^-\pi^+\pi^-$ events that are photoproduced to those that are neutral-hadron induced. While in the raw data only 15% of the events with one or more K's are from a photon in the beam, two-thirds of the events in the final sample are photoproduced.

TABLE IV. Percentage of events photoproduced (calculated from data).

Trigger	25%
≥ 1 K events	18%
"Diffractive" tapes	47%
Diffractive tapes, ≥ 1 K	47%
Diffractive tapes with cuts (5π)	69%
Diffractive tapes with cuts ($KK\pi\pi$)	67%

C. Background subtractions and corrections

Table IV lists the percentage of events calculated to be photoproduced at various stages of the analysis. The estimate of hadronic contamination is made as discussed in Sec. II H. Table III lists the candidate events in each final state after all cuts have been made. The number of events of the regular tapes (N_γ) and background tapes (N_K) are listed. Also shown are the resonance efficiency parameters (ϵ_R) which were calculated separately on each data sample. The relative normalization of the regular and background data is called C. The resulting number of photoproduced events for each channel is $N_{\mathrm{ev}} \pm \sigma$, where $N_{\mathrm{ev}} = N_\gamma \epsilon_R - C N_K \epsilon_R$.

In Table V is the acceptance A' for each state.

TABLE V. Corrections by state.

State	N_{ev}	A'	$A'\epsilon_T$	B	$\sigma(\ )/\sigma(\to KK\pi\pi)$
$\phi\pi\pi$	72.9	18.4	9.1	0.49	0.091 ± 0.017
$K^{*0}K^{\mp}\pi^{\mp}$	212.4	12.5	6.9	0.67	0.26 ± 0.030
$K^+K^-\rho^0$	167.3	11.6	6.9	1.00	0.13 ± 0.01
$K^+K^-\pi^+\pi^-$	1455	13.7	8.1	1.00	1.00
$K^{*\pm}K^{\mp}$	5.0	1.6	0.68	0.11	0.37 ± 0.27
$K^{*0}K_s$	7.6	1.8	0.77	0.23	0.24 ± 0.07
$K^\pm\pi^\mp K_s$	42.2	3.3	1.5	0.34	0.46 ± 0.16
$\omega\pi^+\pi^-$	685	9.9	4.6	0.89	0.93 ± 0.08
$\eta\pi^+\pi^-$	92.0	6.2	2.7	0.24	0.79 ± 0.08
ωK^+K^-	10.8	2.6	1.5	0.89	0.045 ± 0.013
ηK^+K^-	2.6	1.7	0.9	0.24	0.067 ± 0.026
$\phi\pi^+\pi^-\pi^0$	4.2	4.0	2.4	0.49	0.020 ± 0.011
$K^+K^-\rho\pi^0$	9.4	2.9	1.8	1.00	0.029 ± 0.006
$K^{*0}K^\pm\pi^\pm\pi^0$	7.9	1.8	1.1	0.67	0.060 ± 0.021
$K^+K^-\pi^+\pi^-\pi^0$	100.3	2.7	1.7	1.00	0.33 ± 0.05
$\phi\pi^+\pi^-\pi^+\pi^-$	27.8	6.2	4.7	0.49	0.067 ± 0.013
$K^{*0}K^{\mp}\pi^{\mp}\pi^+\pi^-$	22.7	2.1	1.6	0.67	0.12 ± 0.05
$K^+K^-\rho\pi^+\pi^-$	55.2	5.2	3.8	1.00	0.08 ± 0.01
$K^+K^-\pi^+\pi^-\pi^+\pi^-$	229.7	5.6	4.1	1.00	0.31 ± 0.04
$K^+K^-K^+K^-$	14.4	11.9	7.8	1.00	0.010 ± 0.004
$K^+K^-\phi$	2.9	9.2	6.0	0.49	0.005 ± 0.006
$\phi\phi$	2	15.8	11.8	0.24	

Efficiencies including geometrical acceptance and analysis losses were calculated using the Monte Carlo program described in Sec. III F. Further corrections which are included in A' but were not simulated in the Monte Carlo are losses due to K decay in flight (7% per K), K losses from spurious hits in the Cherenkov counter (5% per K), losses due to photon conversions before the magnet $M2$ (6% per γ), and γ losses from spurious hits in the lead-glass array (5% per γ). The acceptance multiplied by the trigger efficiency (ϵ_T) is also listed.

D. Cross section

Since the relative production for several states is presented in Table V, only the $K^+K^-\pi^+\pi^-$ cross section is calculated here. Cross sections for other processes can be determined by using the ratios in Table V. Certain large systematic errors which enter in the cross-section determination do not affect the ratios.

Calculations have been based on data in a restricted t region. To extract the total diffractive cross section, a correction must be made for the part that was cut out. The differential cross section includes scattering from hydrogen and both coherent and incoherent scattering from carbon

$$\frac{d\sigma}{dt}=Ce^{-at}[N_cA^2e^{-bt}+N_cA(1-e^{-bt})+N_H], \qquad (1)$$

where

a = the slope from a single nucleon and is taken from t-dependent measurements of production; $a=6.5\ \mathrm{GeV}^{-2}$;

b = the slope of the coherent production from a carbon nucleus; $b=60\ \mathrm{GeV}^{-2}$;

C is a normalization constant;

A_c = the atomic number of carbon, 12;

N_h = the number of hydrogens in the target; $N_h=0.52N$;

N_c = the number of carbon atoms in the target; $N_c=0.48N$; and

N = the number of atoms in the target.

The correction in the cross section due to only using events below $t=0.05\ \mathrm{GeV}^2$ is

$$\frac{\sigma}{\sigma_{\text{calc}}}=\frac{\int_0^\infty \frac{d\sigma}{dt}dt}{\int_0^{0.05}\frac{d\sigma}{dt}dt}. \qquad (2)$$

This correction factor is 1.57.

In this experiment, events were counted which were not in fact photoproduced, but were induced by the K_L^0's and neutrons in the beam. These events could be subtracted because the experiment ran one-fourth of the time with the photon beam attenuated, and these events were examined with the same programs that were used on the photon tapes. The relative normalization for the subtraction was fixed by the proton flux and corrected for the hadron loss in the photon attenuator. As a check of this normalization, exclusive production of the $K^*(890)$, which would be expected to be predominantly from the K-longs in the beam, was calculated. The ratio of $K^*(890)$'s on the regular tapes was consistent with the proton flux to the accuracy of the determination of the number of K^*'s, which was about 20%.

Systematic errors are estimated as follows

(i) Errors in the photon flux due to pair production not reaching the quantameter: ±5%;

(ii) Electronic inefficiency of the trigger bit: +10%;

(iii) Uncertainty in level of energy trigger: ±20%;

(iv) Errors in TRM logic: +5%;

(v) Error in shape of photon spectrum: ±5%;

(vi) Uncertainty in mass distribution used in Monte Carlo: +15%, −10%

Including these systematic errors, the diffractive cross section for $KK\pi\pi$ production is $\sigma(\gamma A\to K^+K^-\pi^+\pi^-A)=80^{+35}_{-25}$ nb per nucleon. The reader is reminded that the following assumptions have been made: no nuclear shadowing; energy-independent cross section; t distribution given. Drastically changing any of these assumptions would affect the cross section.

V. RESULTS AND DISCUSSIONS

The results of this study are ratios of several exclusive photoproduction meson states, especially those of interest in studying the OZI rule. For this purpose, we have normalized all the production rates relative to the total production of $KK\pi\pi$ events (including all resonance channels). These ratios are obtained from the data in Table III and are given in Table V. All errors are statistical. Further systematic errors in comparing states with different numbers of K mesons are estimated to be 10%. Comparisons of states with different numbers of neutral particles are estimated to have a systematic error of 20%. Systematic errors in comparing states with the same observed particles, in the final state are less than 5%.

A. Tests of the OZI rules

Two possible quark-line diagrams for $\phi\pi\pi$ production are shown in Figs. 22(a) and 22(b). It is seen that these are both "disconnected" diagrams and therefore suppressed by the OZI rule. A dia-

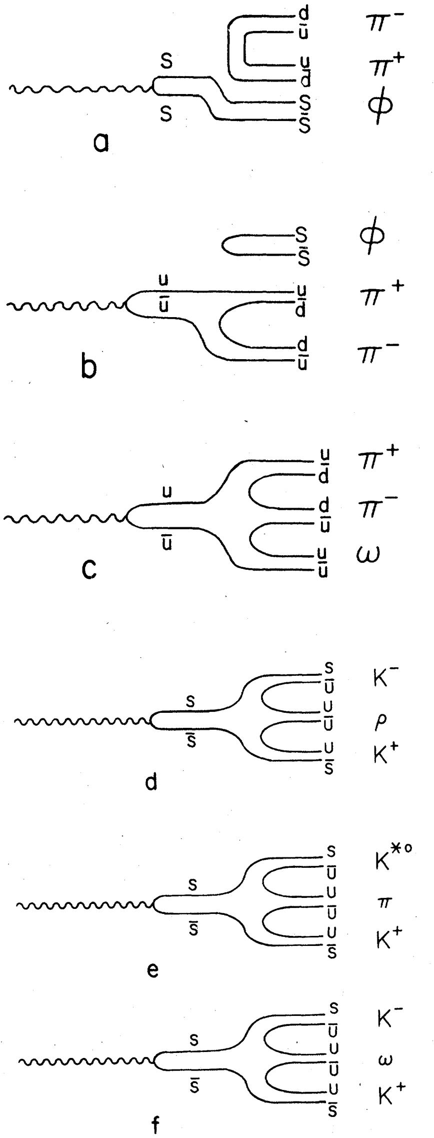

FIG. 22. Quark-line diagrams for various processes.

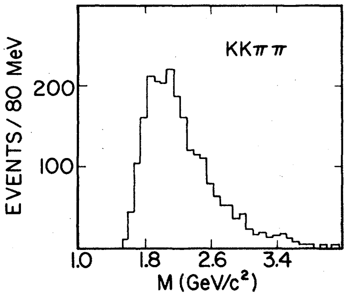

FIG. 23. $KK\pi\pi$ mass distribution after all cuts.

gram for $\omega\pi\pi$ production is shown in Fig. 22(c). This diagram is a normal connected diagram.

Previous tests of the OZI rule in production processes have been reviewed by Okubo.[13] Most of these tests involve comparison of ω and ϕ production in various exclusive channels using pion, proton, and antiproton beams.[16-18] The evidence is that the OZI-rule-forbidden processes are typically no more than 2% of the allowed processes. Without any OZI suppression factor, one might expect the ratio to be unity since the quantum numbers are the same and phase space is fairly similar. The result obtained for this photoproduction experiment is that $\sigma(\gamma\rightarrow\phi\pi^+\pi^-)/\sigma(\gamma\rightarrow\omega\pi^+\pi^-)=0.097 \pm .019$. This is an appreciably larger number than 2% and represents less suppression than has been seen in the production of these states by hadrons. Rather interestingly, it is also similar to the result that is obtained in ψ decay which has an unexpectedly large ratio $\phi\pi\pi/\omega\pi\pi=0.2$. One possibility that was raised for the ψ decay was that the $\pi^+\pi^-$ mass distribution might show some type of resonance or final-state interaction. However, the $\pi^+\pi^-$ distribution in $K^+K^-\pi^+\pi^-$, $\phi\pi^+\pi^-$, and $\omega\pi^+\pi^-$ were all similar in our data.

The $\phi\pi\pi/\omega\pi\pi$ ratio is a function of the mass interval ($M_{\phi\pi\pi}$ and $M_{\omega\pi\pi}$) used. Specifically, if we increase the threshold above which we compare masses, we find that the ratio increases, namely using masses above 1.8 GeV the ratio rises to 18%. For masses greater than 2.2 GeV/c^2, the ratio is 26%. The $K^+K^-\pi^+\pi^-$ mass distribution, given in Fig. 23, is qualitatively similar for every channel studied.

The $\phi\pi^+\pi^-$ final state is the only one reported in this paper which cannot be drawn with at least one connected diagram. Other final states which include strange particles, such as $KK\rho$, $K^*K\pi$, and ϕKK can be drawn with connected diagrams as shown in Figs. 22(d)–22(f). It is therefore also of interest to compare the ratios of $\phi\pi\pi$ to $K^*K\pi$ and $\phi\pi\pi$ to $KK\rho$. All have the same final four particles, two kaons and two pions, and all three states contain a vector meson and two pseudoscalars. The ratios obtained are $\phi\pi\pi/K^*K\pi=0.35 \pm 0.07$ and $\phi\pi\pi/KK\rho=0.68\pm0.14$ and are quite different from zero. There is no large suppression observed in the $\phi\pi\pi$ state, the one with the disconnected diagram.

The ratio $\phi KK/K^*K\pi=0.019\pm0.021$ indicates that there may be a penalty factor for the production of additional strange quarks, which would be formed in pairs out of the vacuum.

In trying to understand the possible origin of suppression for $\phi\pi\pi$ production, we need to distinguish between the quark-line diagrams shown in Figs. 22(a) and 22(b). Figure 22(b) is an example of a hairpin diagram in which the quark-antiquark pair within a single meson are connected. Most hadroproduction experiments have studied the OZI rule with processes represented by this type of diagram. In many models the photon is thought to interact strongly as a quark-antiquark state. Therefore the possibility of strange quarks in the initial state in photoproduction leads to the diagram in Fig. 22(a) which, though disconnected, is not a hairpin diagram.

G parity is a good quantum number in the $\phi\pi\pi$ and $\omega\pi\pi$ final states. The production of both $\phi\pi\pi$ and $\omega\pi\pi$ proceed through the isoscalar portion of the photon, which is $\frac{2}{3}$ strange quarks in the vector-dominance model. The strange quarks have a lower cross section so that the visible isoscalar portion of the photon is about 50% $s\bar{s}$ and 50% normal quarks. Thus the suppression of $\phi\pi\pi$ in Fig. 22(b) may be due to a penalty factor for the strong production of strange quarks, but Fig. 22(a) differs from $\omega\pi\pi$ in Fig. 22(c) only by lack of a connection between the ϕ and the two π's.

Our result may be evidence that disconnected diagrams of the nonhairpin type are only suppressed a factor of 10 relative to connected diagrams. Previous experiments have measured the suppression factor for hairpin diagrams to be much larger (about 100). Both suppression factors could be a consequence of the same OZI rule. This behavior has been suggested on the basis of analyzing crossed channels of OZI-forbidden diagrams.[12]

Lipkin has suggested[19] that due to the *G* parity of the final state, the measured ratio

$$(\phi\pi^+\pi^-\pi^0)^2/(\phi\pi^+\pi^-)\times(\phi\pi^+\pi^-\pi^+\pi^-)\simeq 0.1$$

tests the relative contribution of hairpin diagrams since $\phi\pi^+\pi^-\pi^0$ only has contributions from a hairpin diagram. This ratio would be close to one if diagrams 22(a) and 22(b) had a similar strength. The low value for this ratio supports a larger suppression for hairpin diagrams.

Theoretical predictions have been made that $\sigma(e^+e^-\rightarrow\phi\pi\pi)$ should be very suppressed. As the e^+e^- reaction proceeds via a single photon, coherent photoproduction should be closely related to this process. Our results obtained in this experiment disagree with at least one of these two statements. Our general conclusion is that in photon production reactions we do not see the full suppression expected from the OZI rule.

ACKNOWLEDGMENTS

Several of us wish to acknowledge helpful discussions with Dr. Harry Lipkin. We also wish to acknowledge the support of the staffs of Nevis Laboratory, the University of Illinois Physics Department, and the Proton Department at Fermilab. This research was supported in part by the National Science Foundation and the U. S. Department of Energy.

---

*Present address: Massachusetts Institute of Technology, Cambridge, Massachusetts.

†Present address: Fermi National Accelerator Laboratory, Batavia, Illinois.

‡Present address: Scientific Applications, Inc. NW, Bellevue, Washington.

§Operated by Universities Research Association, Inc. under contract with the U. S. Department of Energy.

[1] G. Zweig, CERN Reports Nos. TH401 and TH412, Geneva, Switzerland 1964 (unpublished).

[2] S. Okubo, Phys. Lett. 5, 165 (1963).

[3] J. Iizuka, Prog. Theor. Phys. Suppl. 37–38, 21 (1966).

[4] J.-E. Augustin *et al.*, Phys. Rev. Lett. 32, 1406 (1974).

[5] J. J. Aubert *et al.*, Phys. Rev. Lett. 33, 1404 (1974).

[6] S. W. Herb *et al.*, Phys. Rev. Lett. 39, 252 (1977).

[7] K. Ueno *et al.*, Phys. Rev. Lett. 42, 486 (1979).

[8] S. Okubo, Phys. Rev. D 16, 2336 (1977).

[9] A. Etkin *et al.*, Phys. Rev. Lett. 41, 784 (1978).

[10] C. W. Akerlof *et al.*, Phys. Rev. Lett. 39, 861 (1977).

[11] M. Binkley *et al.*, Phys. Rev. Lett. 39, 578 (1976).

[12] H. Lipkin, in *New Fields in Hadronic Physics*, proceedings of the XIth Rencontre de Moriond, Flaine-Haute-Savoie, 1976, edited by J. Trân Thanh Vân (CNRS, Paris, 1976), p. 327.

[13] S. Okubo, Phys. Rev. D 14, 108 (1976).

[14] F. Harris and D. Yount, Nucl. Instrum. Methods 114, 357 (1974).

[15] R. Yamada *et al.*, Nucl. Instrum. Methods 138, 567 (1976).

[16] R. A. Donald *et al.*, Phys. Lett. 61B, 210 (1976).

[17] D. S. Ayres *et al.*, Phys. Rev. Lett. 32, 1463 (1974).

[18] V. Blobel *et al.*, Phys. Lett. 59B, 88 (1975).

[19] H. Lipkin, private communication.